

Structure Function Estimated From Histological Tissue Sections

Aiguo Han, *Member, IEEE*, and William D. O'Brien Jr., *Life Fellow, IEEE*

Abstract—Ultrasonic scattering is determined by not only the properties of individual scatterers but also the correlation among scatterer positions. The role of scatterer spatial correlation is significant for dense medium, but has not been fully understood. The effect of scatterer spatial correlation may be modeled by the structure function as a frequency-dependent factor in the backscatter coefficient (BSC) expression. The structure function has been previously estimated from the BSC data. The aim of this study is to estimate the structure function from histology to test if the acoustically estimated structure function is indeed caused by the scatterer spatial distribution. Hematoxylin and eosin stained histological sections from dense cell pellet biophantoms were digitized. The scatterer positions were determined manually from the histological images. The structure function was calculated from the extracted scatterer positions. The structure function obtained from histology showed reasonable agreement in the shape but not in the amplitude, compared with the structure function previously estimated from the backscattered data. Fitting a polydisperse structure function model to the histologically estimated structure function yielded relatively accurate cell radius estimates (error < 15%). Furthermore, two types of mouse tumors that have similar cell size and shape but distinct cell spatial distributions were studied, where the backscattered data were shown to be related to the cell spatial distribution through the structure function estimated from histology. In conclusion, the agreement between acoustically estimated and histologically estimated structure functions suggests that the acoustically estimated structure function is related to the scatterer spatial distribution.

Index Terms—Acoustic scattering, backscatter coefficient, histology, quantitative ultrasound, structure function.

I. INTRODUCTION

QUANTITATIVE ultrasound (QUS) imaging has been extensively researched for the ability of tissue characterization. Earlier QUS successes for tissue characterization involved various organs such as the eye [1], [2], prostate [3], kidney [4], heart [5], [6], blood [7], [8], breast [9]–[12], liver [13], cancerous lymph nodes [14], and apoptotic cells [15], [16]. Recent development in QUS has expanded to clinical settings. Clinical studies showed that QUS approaches are successful for breast cancer treatment monitoring [17], liver fat quantification [18], [19], and breast cancer characterization [20].

QUS seeks to use the frequency-dependent information of the radio-frequency (RF) echo signals backscattered from tissue

to estimate tissue features and properties such as scatterer size, shape, number density, mass density, and acoustic impedance. Tissue property estimation is achieved using a model-based approach, i.e., using an acoustic scattering model that describes the scattering based on tissue microstructure. The accuracy of the underlying scattering model is critical to the success of QUS, while the development of accurate QUS models depends on a clear understanding of acoustic scattering mechanisms in various tissue types.

Physical principles suggest that acoustic scattering from discrete scatterers can be factored into two major components. One component is called the form factor that is determined by the properties of individual scatterers relative to the background [21]. The other component is referred to as the structure factor or structure function that is determined by the spatial distribution of scatterers [22]–[29]. The form factor has been studied extensively, and many models have been developed and applied to various biological tissues. A few representative form factor models include the fluid-filled sphere model [21], the Gaussian model [21], the spherical shell model [21], and the concentric sphere model [10], [30], [31]. The structure function, on the other hand, has not been sufficiently studied in the context of tissue scattering modeling although it can have a strong effect on scattering and is not negligible particularly when the scatterer concentration is high or scatterers are clustered. Therefore, this paper focuses on the study of structure function.

The concept of structure function was originally developed in statistical mechanics, and was first introduced to the field of acoustic scattering in [22] and [32]. Fontaine *et al.* first implemented this concept for describing biological scatterers [23]. Twersky described a theoretical structure function expressed as a function of the correlation length between scatterers, whereas Fontaine *et al.* expanded this concept using a Fourier transform of the individual scatterer positions and validated the concept with the experimental data. The structure function has been used in ultrasound blood characterization to address the difficulty of modeling aggregated cells [24], [33]. To study the effect of spatial distribution of scatterers on the backscattered signal, Monte Carlo studies were performed to simulate two-dimensional (2-D) and three-dimensional (3-D) scatterer position distributions [34]–[36]. In addition, Franceschini *et al.* [37] conducted the experiments on concentrated tissue-mimicking phantoms and modeled the structure function using the Percus–Yevick [38] approximation. The results showed that the scattering models that took into account the Percus–Yevick structure function agreed better with the backscattered data than models that neglected the structure function. However, the phantom study dealt with comparison between the experimental

Manuscript received January 10, 2016; accepted March 21, 2016. Date of publication March 25, 2016; date of current version September 12, 2016. This work was supported by the National Institutes of Health under Grant R01CA111289 and Grant R01DK106419.

The authors are with the Bioacoustics Research Laboratory, Department of Electrical and Computer Engineering, University of Illinois, Urbana, IL 61801 USA (e-mail: wdo@uiuc.edu).

Digital Object Identifier 10.1109/TUFFC.2016.2546851

backscatter coefficient (BSC) and the model BSC, where the effects of the structure function and form factor could not be separated. To more directly study the structure function in a previous study, we performed cell pellet biophantom experiments to extract the structure function from BSC [39]. In that study, two concentrations of biophantoms were constructed: a lower concentration and a higher concentration. The lower concentration cell pellet biophantom was designed to be sufficiently sparse such that the interaction among scatterers could be neglected and the structure function could be assumed to be unity. The higher concentration biophantom was designed to mimic tumors, where the cells were densely packed. The form factor was assumed to be the same for the lower concentration and higher concentration biophantoms. Then, the structure function of the higher concentration biophantom was extracted by comparing the BSCs of the two concentrations. The extracted structure function was in agreement with the theoretical structure function models developed in that study.

In this paper, we will develop the algorithms for estimating the structure function from the histology of biophantoms and compare the histologically estimated structure function to that estimated acoustically, as was done in [25]. Three-dimensional histological data have been used by Mamou *et al.* to model and identify scattering structures [40], [41]. In [40] and [41], 3-D acoustic impedance maps (3DZMs) were created based on digitized histological images. The 3DZMs allow one to consider 3-D structures and polydisperse media to predict the scattered power spectrum. The 3DZM approach made it possible to connect ultrasound data with the actual 3-D structure of the tissue under investigation. Inspired by the 3DZM approach, this paper investigates the structure function using 2-D histological images. Specifically, the aim is to investigate whether the acoustically estimated structure function in [25] was indeed a result of the spatial distribution of scatterers. This investigation is helpful in improving our understanding of the relationship between the backscattered data and histology. As an example, we will apply the histological structure function algorithm to two mammary tumor types: a mouse carcinoma (4T1, ATCC #CRL-2539), and a mouse sarcoma [Englebret-Holm-Swarm (EHS), ATCC #CRL-2108], to demonstrate how the backscattered data are related to the spatial distribution of cells as determined using hematoxylin and eosin (H&E) histology. The two types of tumor cells have similar cell morphology but different spatial distributions, and are ideal examples for the purpose of studying the structure function.

This paper is organized as follows. The structure function theory will be reviewed in Section II. Section III will describe the experimental procedure for preparing the biophantom and tumor samples, and the algorithm for estimating the structure function from histological sections. Section IV will review the structure function results obtained acoustically for the biophantoms in [24], and present the histologically estimated results, and compare the two. The histologically estimated structure function is then compared to a polydisperse structure function model developed in [25]. The structure function results from tumors will also be presented. Several issues in the results will be discussed as well. Section V concludes this paper.

II. STRUCTURE FUNCTION THEORY

A. Backscatter Coefficient

Consider a plane wave of unit amplitude incident on a scattering volume V that contains N discrete scatterers. The total scattered field far from the scattering volume behaves as a spherical wave [21, eq. (4)]

$$p_s(\mathbf{r}) = \frac{e^{ikr}}{R} \sum_{j=1}^N \Phi_j(\mathbf{K}) e^{i\mathbf{K}\cdot\mathbf{r}_j} \quad (1)$$

where \mathbf{r} is the observation position with respect to the origin $R = |\mathbf{r}|$, \mathbf{r}_j is the position of the j th scatterer, and k is the propagation constant ($k = \omega/c$, where ω is the angular frequency and c is the propagation speed). The factor $\Phi_j(\mathbf{K})$ is the complex scattering amplitude of the j th scatterer and describes the spatial frequency dependence of the scattered pressure; Φ_j is a function of the scattering vector \mathbf{K} whose magnitude is given by $|\mathbf{K}| = 2k \sin(\theta/2)$, where θ is the scattering angle ($\theta = \pi$ for backscattering). Φ_j is dependent on the scatterer size, shape, and acoustic properties.

The differential cross section per unit volume σ_d (i.e., the power scattered into a unit solid angle observed far from the scattering volume divided by the product of the incident intensity and the scattering volume) may be expressed as

$$\sigma_d(\mathbf{K}) = \frac{R^2 I_s}{V I_0} = \frac{1}{V} \left| \sum_{j=1}^N \Phi_j(\mathbf{K}) e^{i\mathbf{K}\cdot\mathbf{r}_j} \right|^2 \quad (2)$$

where I_s and I_0 denote the scattering intensity and incident intensity, respectively, and $|\cdot|^2$ represents the squared modulus of the quantity.

BSC is defined as the differential cross section per unit volume in the backscattering direction ($|\mathbf{K}| = 2k$).

B. Structure Function

If the scatterers are spatially uncorrelated (which often occurs when the scattering volume contains a sparse concentration of scatterers without clustering), the phase terms $e^{i\mathbf{K}\cdot\mathbf{r}_j}$ in (2) may be assumed to be uncorrelated. The differential cross section per unit volume for this case is denoted by $\sigma_{d,\text{incoherent}}$, and may be expressed as

$$\sigma_{d,\text{incoherent}}(\mathbf{K}) = \frac{1}{V} \sum_{j=1}^N |\Phi_j(\mathbf{K})|^2. \quad (3)$$

If the scatterers are spatially correlated, and the scattering amplitudes $\Phi_j(\mathbf{K})$ are identical for all the scatterers, then (2) may be simplified as

$$\sigma_d(\mathbf{K}) = \bar{n} |\Phi_j(\mathbf{K})|^2 \frac{1}{N} \left(\sum_{j=1}^N e^{i\mathbf{K}\cdot\mathbf{r}_j} \right) \left(\sum_{j=1}^N e^{-i\mathbf{K}\cdot\mathbf{r}_j} \right) \quad (4)$$

where $\bar{n} = \frac{N}{V}$ is the number density of the scatterers. Dividing (4) by (3) yields the structure function

TABLE I
ASSUMPTIONS ABOUT THE INDIVIDUAL SCATTERERS FOR THE THREE
STRUCTURE FUNCTION MODELS DISCUSSED IN [25]

Model name	Scatterer size distribution	Scattering amplitude of individual scatterers	Form factor
Monodisperse model	Same size	Same amplitude	N/A
Polydisperse model I	Γ - (Schulz-) distribution	Same amplitude	N/A
Polydisperse model II	Γ - (Schulz-) distribution	Different amplitudes	Fluid-fill spheres

N/A means no form factor is assumed.

$$S(\mathbf{K}) = \frac{1}{N} \left(\sum_{j=1}^N e^{i\mathbf{K}\cdot\mathbf{r}_j} \right) \left(\sum_{j=1}^N e^{-i\mathbf{K}\cdot\mathbf{r}_j} \right) = \frac{1}{N} \left| \sum_{j=1}^N e^{-i\mathbf{K}\cdot\mathbf{r}_j} \right|^2. \quad (5)$$

If the exact position of each scatterer is known, the structure function can be calculated deterministically using (5). Therefore, (5) is useful for numerically calculating the structure function from histology. A structure function of unity corresponds to uncorrelated random scatterer positioning, and the structure function values above unity means constructive interferences whereas the values below unity means destructive interferences due to the scatterer positioning.

If the positions of individual scatterers are unknown, the structure function can still be calculated from the distribution function of the scatterers. Different scatterer distribution function models will result in different structure function models. Also, the structure function can be affected by the scatterer size distribution. Three Percus–Yevick type structure function models based on different assumptions about the scatterer size and scattering amplitude were discussed in [25]: the monodisperse model, polydisperse model I, and polydisperse model II. The assumptions for the three models are listed in Table I. It was shown in [25] that the two polydisperse structure function models agree with the acoustically estimated structure function in dense cell pellets. The polydisperse model I will be used in this study to evaluate the histologically estimated structure function because it is mathematically simpler than polydisperse model II and does not require a form factor. In polydisperse model I, the scatterers are assumed to be nonoverlapping spheres. The probability density function of the scatterer radius is assumed to follow a Γ - (Schulz-) distribution with a probability density function [25]

$$f_z(x) = \frac{1}{z!} \left(\frac{z+1}{a} \right)^{z+1} x^z e^{-\frac{(z+1)x}{a}}, \quad z = 0, 1, 2, \dots \quad (6)$$

where a is the mean of the scatterer radius, and z is the Schulz width factor, which is a measure of the width of the distribution (a greater z value represents a narrower distribution). The structure function is expressed as a function of mean sphere radius a , Schulz width factor z , wavenumber k , and sphere volume fraction η . The detailed analytical expression of the structure function for the model is available in [25, Appendix A].

III. EXPERIMENTS AND METHODS

A. Experiment Overview

This paper presents two experiments, one using biophantoms, the other using *ex vivo* tumors. The biophantom experiment is a continuation of the experiment described in [25]. In [25], three sets of biophantoms were constructed, with each set having two cell concentrations. Different sets of biophantoms were made from different cell lines, whereas the two concentrations of the same set were made from the same cell line. The biophantoms were composed of a known number of cells clotted in a mixture of bovine plasma (Sigma-Aldrich, St. Louis, MO, USA) and bovine thrombin (Sigma-Aldrich, St. Louis, MO, USA). Three cell lines were used to create the cell pellet biophantoms: Chinese hamster ovary [CHO, American Type Culture Collection (ATCC) #CCL-61, Manassas, VA, USA], 13762 MAT B III (MAT, ATCC #CRL-1666), and 4T1 (ATCC #CRL-2539). The mean cell radii for CHO, MAT, and 4T1 were 6.7, 7.3, and 8.9 μm , respectively, and the estimated Schulz width factor z for CHO, MAT, and 4T1 were 51.9, 65.8, and 31.9, respectively, based on light microscope measures [25]. The structure function was estimated from the BSC for the high-concentration biophantoms in [25]. This paper utilizes the histology slides stained with H&E from those biophantoms for structure function estimation.

For the tumor experiment, 4T1 and EHS *ex vivo* tumor samples were scanned using three single-element, weakly focused transducers (20-MHz transducer IS2002HR, from Valpey Fisher Cooperation, Hopkinton, MA, USA; 40- and 80-MHz transducers from NIH High-frequency Transducer Resource Center, University of Southern California, Los Angeles, CA; same as those used in [25]). The total frequency range covered was 11–105 MHz. The BSC was estimated using the same planar reference technique as that used in [25]. H&E-stained histological slides from the tumors were used for the structure function estimation.

B. Tumor Sample Preparation

The 4T1 and EHS cells were injected into BALB/c mice and C57BL/6 mice, respectively, to grow into tumors. All animals were purchased from Harlan Laboratories, Inc. (Indianapolis, IN, USA). The animals were euthanized via CO_2 , and the tumors were immediately excised. The excised tumors were trimmed such that the thickness did not exceed 2 mm. This was done to reduce total attenuation and achieve a good signal-to-noise ratio for the insertion-loss attenuation measures that were needed for BSC calculation. The excised tumors were placed on a planar Plexiglas plate immediately after the trimming was performed. The tumors and the Plexiglas plate were submerged in DPBS for ultrasonic scanning. 15 4T1 and 13 EHS tumors were successfully excised, scanned, and analyzed. The tumor scanning was performed using the same setup and by the same operator during a period of a few weeks. Note that the attenuation and BSC results for the 15 4T1 tumor samples have been published in [39].

The experimental protocol was approved by the Institutional Animal Care and Use Committee of the University of Illinois

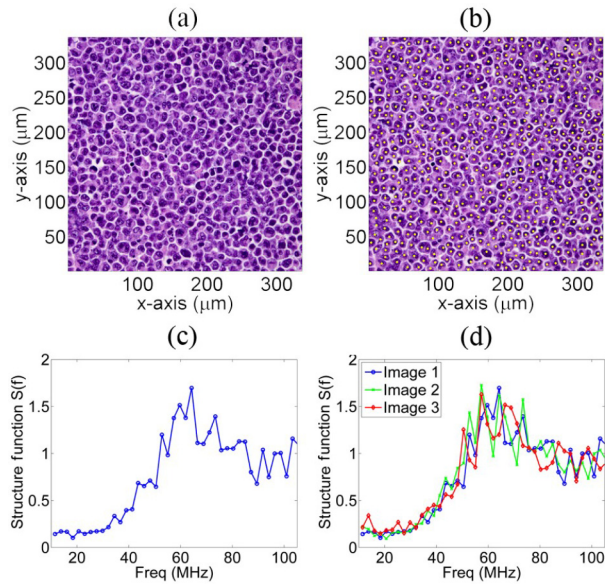


Fig. 1. Step-by-step procedure for estimating the structure function from histology. (a) Original H&E image. (b) Scatterer positions determined from the H&E image. (c) Resulting structure function versus frequency calculating from one image. (d) Structure function curves calculated from three images. Data shown in (a)–(c) were from a 4T1 cell pellet biophantom sample.

and satisfied all campus and National Institutes of Health rules for the humane use of laboratory animals. Animals were housed in an Association for Assessment and Accreditation of Laboratory Animal Care (Rockville, MD, USA)-approved animal facility and provided food and water *ad libitum*.

C. Histology Processing

Immediately after scanning, the sample was placed into a histology processing cassette and fixed by immersion in 10% neutral-buffered formalin (pH 7.2) for a minimum of 12 h for histopathologic processing. The sample was then embedded in paraffin, sectioned, mounted on glass slides, and stained with H&E for further evaluation by light microscopy (Olympus BX-51, Optical Analysis Corporation, Nashua, NH, USA).

D. Structure Function Estimation From Histology

An H&E-stained tissue section was viewed under the light microscope. For each tissue slide, a TIF format picture was taken using the digital camera that was connected with the microscope. The magnification of the objective lens was $40\times$. The digitized image had a size of 1920×1920 pixels, with a resolution of 5.72 pixels per micron. Therefore, the image covered an area of $336 \times 336 \mu\text{m}^2$. For each scanned biological sample type, multiple pictures from separate histological sections were taken and analyzed. An example of the digitized image is shown in Fig. 1(a).

A custom MATLAB routine was developed to allow manual determination of the cell center for each cell on the image. The manual determination process was completed by clicking on the visually inspected cell center of the image that

was opened in MATLAB [Fig. 1(b)]. The cell center coordinates were automatically recorded. The 2-D form of (5) was then used to calculate the structure function from the recorded cell centers [42]. Specifically, the wave vector was chosen as $\mathbf{K} = \frac{2\pi}{L}(n_x\hat{x} + n_y\hat{y})$, with the magnitude $k = \frac{2\pi}{L}\sqrt{n_x^2 + n_y^2}$, where $n_x, n_y = 0, \pm 1, \pm 2, \dots$, and L is the side of the image ($336 \mu\text{m}$). A radial averaging was then performed with a resolution of $2\pi/L$ for k . For backscattering, the spatial frequency $k = |\mathbf{K}|$ was converted to temporal frequency f by the relationship $f = \frac{kc}{4\pi}$, where c was the speed of sound, and was assumed to be 1540 m/s. The resulting structure function as a function of temporal frequency f was the final structure function estimated from one image [Fig. 1(c)]. The procedure for estimating the structure function from histology was repeated for three images per sample type. For example, the estimated structure function curves from three histological images for the 4T1 cell pellet biophantom is shown in Fig. 1(d). The curves from the three images were averaged to yield the final histologically estimated structure function for a sample type.

E. Structure Function Model Fitting

The polydisperse model I introduced in Section II-B was fitted to the histologically estimated structure function of the cell pellet biophantoms to yield the scatterer size estimates. The mean radius a and the Schulz width factor z were the unknowns. The volume fraction was assumed to be known *a priori* ($\eta = 74\%$). The two unknowns were estimated by fitting the theoretical structure function $SF_{\text{theo}}(f)$ predicted by polydisperse model I to the histologically estimated structure function $SF_{\text{hist}}(f)$. Specifically, an exhaustive search procedure was performed for values of $(a, z) \in [1 \mu\text{m}, 100 \mu\text{m}] \times [1, 100]$ to minimize the cost function

$$C(a, z) = \sum_i \|SF_{\text{theo}}(f_i) - SF_{\text{hist}}(f_i)\|^2 \quad (7)$$

over the frequency range 11–105 MHz.

To explore the effect of potential bias caused by assuming a volume fraction of 74%, various volume fraction values, ranging from 0.65 to 0.85, were also assumed in the least squares estimation, although some of the assumed volume fraction values might be beyond the limit of the model assumptions regarding hard sphere packing.

F. Simulation

A set of simulations was performed to evaluate the bias of using the 2-D structure function to infer the 3-D structure function. The basic idea was to generate a 3-D random distribution of spheres, calculate from the 3-D random distribution both the 3-D and the 2-D structure functions using (5), and make a comparison between 2-D and 3-D.

In each simulation, a large number of spheres were generated. The radii of the spheres followed a Γ -distribution (6), with $a = 6.7 \mu\text{m}$, and $z = 51.9$, to match the cell radius distribution of the CHO cells. The spheres were randomly distributed in a cube of a given size ($400 \mu\text{m} \times 400 \mu\text{m} \times 400 \mu\text{m}$). No

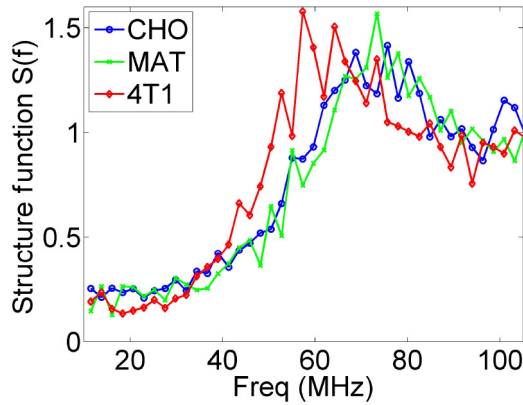


Fig. 2. Comparison among the estimated structure functions from the histological sections for high-concentration CHO, MAT, and 4T1 cell pellet biophantoms. Each curve is an average of three-independent measures from different histological images of the same cell type.

sphere overlapping was allowed. The periodic boundary condition was used. The volume fraction of the spheres varied from simulation to simulation. The volume fractions generated were 10%, 20%, 30%, and 60%. The simulations of volume fractions higher than 60% were not performed due to the difficulty of generating random distributions of the spheres at a very high volume fraction.

Two algorithms were used to generate the random sphere distributions: the Metropolis algorithm [43] for the 10%, 20%, and 30% volume fractions, and the forced-biased algorithm [44] for the 60% volume fraction. The Metropolis algorithm generates sphere distributions that are consistent with the Percus–Yevick approximation, and hence the polydisperse model I. However, this algorithm is only suitable for a relatively low volume fraction generation. It becomes increasingly slow as the volume fraction increases. The force-biased algorithm is suitable for high volume fraction generation, but it generates a distribution that is not the same as that described by polydisperse model I. The force-biased algorithm used in the present study was slightly modified from the version described in [43] to generate a sphere distribution for a given volume fraction. The version in [43] was intended to generate the highest packing density. It starts with an initial configuration that allows overlaps, and then attempts to reduce overlaps in every iterations by two operations: pushing apart overlapping spheres by choosing new positions, and gradual shrinking the spheres. The shrinking step [43, eq. (5)] was omitted in our implementation.

IV. RESULTS AND DISCUSSION

A. Histologically Estimated Structure Function for Biophantoms

The histologically estimated structure function curves are presented in Fig. 2 for high-concentration cell pellet biophantoms of three cell lines: CHO, MAT, and 4T1. Each of the curves was the average of three realizations (i.e., measurements from three different images).

None of the curves in Fig. 2 are constant across the frequency range plotted. The curves have a maximum-and-minimum

structure, with a peak around 70 MHz, and a minimum around 30 MHz. The structure function at the peak is higher than unity and at the minimum is lower than unity. This suggests that the scatterer position distribution does have an influence on the backscattered power spectrum. The scatterer position distributions for these high-concentration biophantoms exhibit similarly destructive interference effects and constructive interference effects. These results are expected, because the cells are tightly packed in the high-concentration biophantoms such that the scatterer positions are highly correlated. The correlation should be related to the cell diameters. Theoretically, a larger scatterer diameter corresponds to a lower constructive frequency if the scatterers are tightly packed. The peak of the structure function occurs for a product ka between 1.5 and 2 for tightly packed spheres [25, Fig. 2]. Fig. 2 shows that the 4T1 has the lowest peak frequency in the structure function curve out of the three cell lines, which is consistent with the fact that 4T1 has the largest cell radius out of the three (8.9 μm , compared to 6.7 μm for CHO and 7.3 μm for MAT).

B. Comparison Between Histologically Estimated and Acoustically Estimated Structure Functions for Biophantoms, and Polydisperse Structure Function Model Fit

The structure function curves estimated histologically are compared to the acoustically estimated curves that were published in [25, Fig. 7]. Fig. 3 shows such a comparison for each cell line individually. The acoustically estimated and histologically estimated curves appear to be similar in the shape for all the cell lines. The peak positions agree well between the two structure function curves for each of the three cell lines. The magnitude agreement is not as good, however. Only MAT shows reasonable agreement in structure function curves [Fig. 3(b)]. For CHO, the acoustically estimated structure function is mostly lower than the histologically estimated structure function across the frequency range [Fig. 3(a)]. The peak magnitude barely exceeds unity for the acoustically estimated structure function for CHO. The 4T1 appears to behave similarly in magnitude to that of the CHO, i.e., the peak magnitude is less than unity.

A number of reasons might have contributed to the difference in the amplitudes of the acoustically estimated structure function and histologically estimated structure function observed in Fig. 3, and the observed difference was expected. From the acoustics side, there could be a slight bias in the acoustically estimated structure function: The structure function estimation using acoustics requires the knowledge of the number densities of both the high- and the low-concentration cell pellet biophantoms. Errors in the number density estimation will be translated into errors in the magnitude of the acoustically estimated structure function curves. From the histology side, the fixation might have changed the sphere distribution and material structures such that the fixed biophantoms did not have exactly the same structure compared to when the biophantoms were being scanned. Also, it can be argued that a 2-D estimation does not perfectly agree with 3-D reality, which might contribute to the magnitude discrepancy as well. The bias caused using the 2-D structure function to estimate the 3-D structure

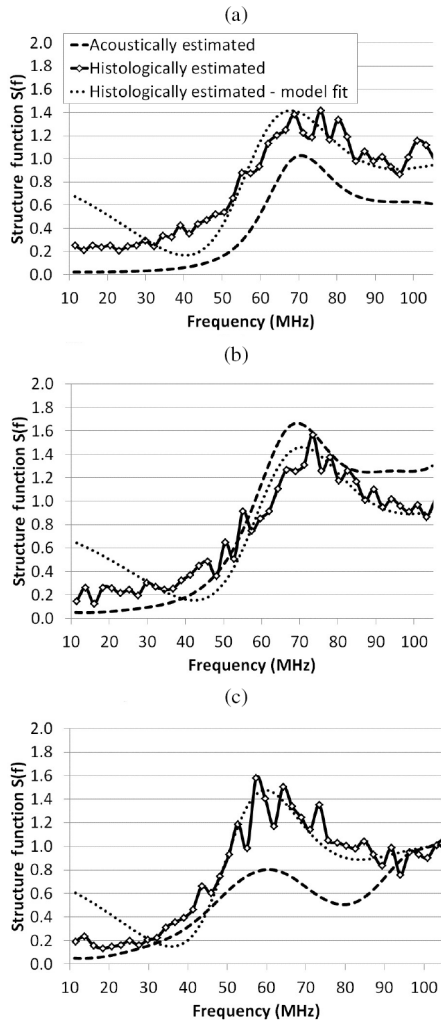


Fig. 3. Comparison between the acoustically estimated and histologically estimated structure function curves for high-concentration (a) CHO, (b) MAT, and (c) 4T1 cell pellet biophantoms. Also presented are the best-fit structure functions to the histologically estimated curves using a polydisperse structure function model. The acoustically estimated curves were adapted from the experimental curves in [25, Fig. 7]. The histologically estimated curves were adapted from Fig. 2.

function is investigated in detail in Section IV-C. Moreover, the method of using cell centers to calculate the structure function implies the assumption of same scattering amplitude for the scatterers (Table I), which could create a bias on the structure function magnitude and frequency dependence. This might explain why the amplitude of the histologically estimated structure function is different than the amplitude of the acoustically estimated structure function, especially for the CHO and 4T1 cells that have smaller Schulz width factors. This observation is consistent with the MAT cell experiments giving the best agreement in structure function curves and having the largest Schulz width factor around 66.

Despite the discrepancy in magnitude, the agreement in the frequency dependence and the positions of the structure function peaks may yield valuable information. Fitting a polydisperse structure function model to the histologically estimated structure function model yielded reasonable cell radius

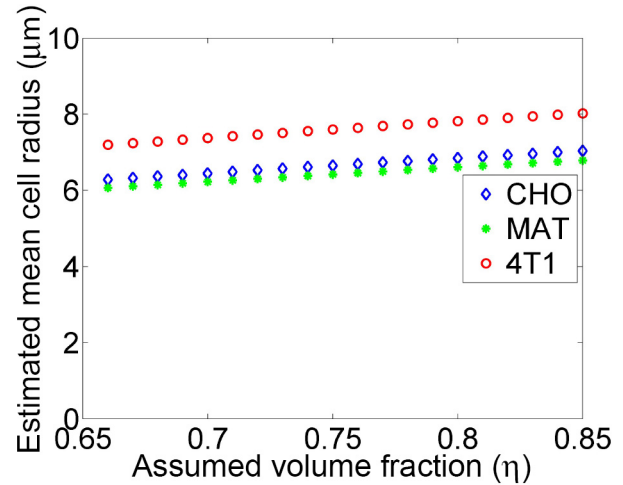


Fig. 4. Estimated mean cell radius versus the assumed volume fraction for CHO, MAT, and 4T1 cell pellet biophantoms.

estimates. The best-fit curves (assuming the volume fraction $\eta = 74\%$) were plotted against the histologically estimated curves in Fig. 3. The estimated mean cell radii were 6.6, 6.4, and 7.6 μm for CHO, MAT, and 4T1, respectively. Those values were slightly underestimated, but were accurate within 15% error compared to the direct light microscope measures (6.7, 7.3, and 8.9 μm for CHO, MAT, and 4T1, respectively; see [25, Fig. 4]). If the assumed volume fraction of 74% is incorrect, then the estimated size would be biased. To demonstrate such a bias, a range of volume fractions was assumed for the size estimation and the estimated radius versus assumed volume fraction is presented in Fig. 4. Fig. 4 suggests that no significant bias in the size estimation would be expected if the 74% volume fraction is biased. The slight underestimation of the cell size was likely caused by the shrinkage because of fixation in preparation for the staining. Neutral-buffered formalin fixation has been shown to reduce the linear dimension of the cells, nuclei, and whole tissue by approximately 10% [45], [46] compared to fresh samples. This amount of shrinkage is consistent with the underestimated cell size using the histologically estimated structure function.

There have been debates in the literature over whether the cell nucleus [47–[50] or the whole cell [41], [51], [52] is the primary scattering source. It is worth pointing out that the agreement we observed in this study between the estimated model parameter a and the cell radius does not necessarily suggest that the whole cells is the primary scattering source if we assume the cell center and the nucleus center overlap for each cell. The question of which entity is the scattering source arises in the context of the form factor. The scatterer radius used in a form factor is not necessarily the same as the radius used in the structure function. The scatterer radius determined by the form factor describes the effective radius based on the impedance distribution, whereas the scatterer radius determined by the structure function is related to the effective interaction length among the scatterers. For the cell pellet case, there is a debate regarding the effective radius based on the impedance distribution, but the interaction length is not ambiguous—it is

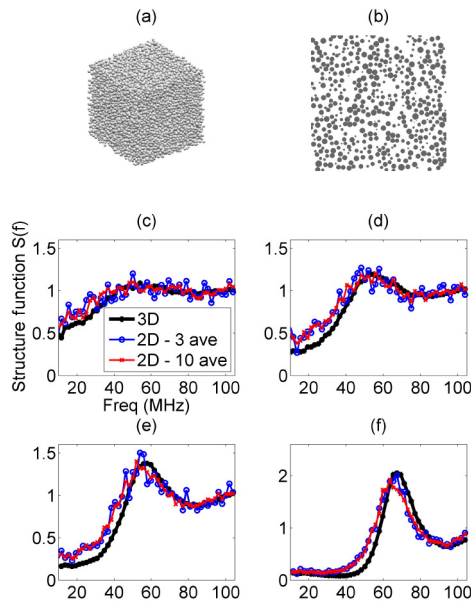


Fig. 5. (a) Example of the simulated 3-D distribution of spheres; (b) 2-D slice obtained from the simulated 3-D distribution; and the calculated 3-D structure function, 2-D structure function with three averages, and 2-D structure function with 10 averages for volume fractions of (c) 10%; (d) 20%; (e) 30%; and (f) 60%.

the cell boundary that determines the spatial distribution of the cells, and thus the cell radius is the parameter a that is used in the structure function model.

C. Simulations of 2-D and 3-D Structure Functions

An example of the generated 3-D distribution of spheres is shown in Fig. 5(a). A 2-D slice obtained from the 3-D distribution is shown in Fig. 5(b). The 3-D structure function was calculated for each of the four volume fractions simulated (10%, 20%, 30%, and 60%). Then, three slices were sampled from the 3-D distribution, and the 2-D structure functions were calculated from the three slices and averaged together. Similarly, the average from 10 slices within the 3-D distribution was obtained. The resulting 3-D structure function, 2-D structure function with three averages, and 2-D structure function with 10 averages were shown for every volume fraction in Fig. 5(c)–(f).

The simulation results suggest that the 2-D and 3-D structure functions obtained from the same 3-D sphere distribution have a similar shape, and a similar frequency position of the structure function peak. However, the 2-D structure function has a greater magnitude than that of the 3-D structure function at frequencies lower than the frequency of the peak. This discrepancy between 2-D and 3-D structure function was also observed in all three cell lines of biophantoms (Fig. 3). In particular, the difference between the acoustically estimated and histologically estimated structure functions of the MAT cell pellet mimics the difference between the 3-D and 2-D structure functions shown in Fig. 5(f). The situation for 4T1 and CHO is more complicated. For 4T1 and CHO, the differences between the acoustically estimated and histologically estimated

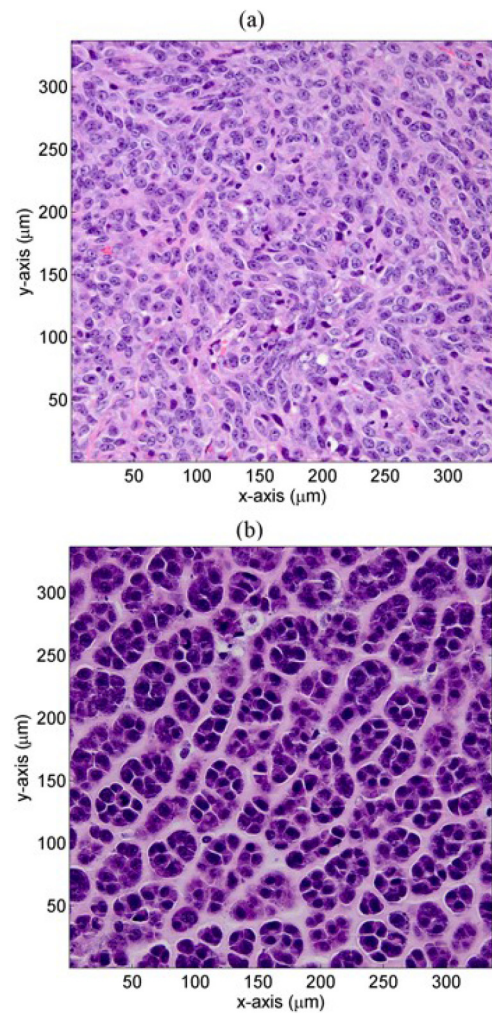


Fig. 6. Optical microscope images (40 \times) of H&E stained (a) 4T1 tumor and (b) EHS tumor histological slides.

structure functions cannot be fully explained by the 2-D versus 3-D simulation. Nevertheless, the simulation demonstrates the power and limitation of using histologically estimated structure function to infer the 3-D structure function. Future research will be pursued to derive the relationship between 2-D and 3-D structure functions to allow for a more accurate estimation of the 3-D structure function using the 2-D structure function.

D. BSC and Histologically Estimated Structure Function for Tumors

The 4T1 and EHS tumor experiments are presented herein to further demonstrate the idea of relating backscattered data to histology through analyzing the scatterer position distribution using structure function. H&E stained histological slides for the two tumor types are shown in Fig. 6. Compared to the 4T1 tumor cells, the EHS tumor cells have a similar size and shape, but different spatial organizations. The 4T1 tumor cells are relatively homogeneously distributed. The EHS tumor cells, however, are grouped into spherical aggregates with an aggregate radius of approximately 20 μm. With this unique structure, the experimentally determined BSC curves for

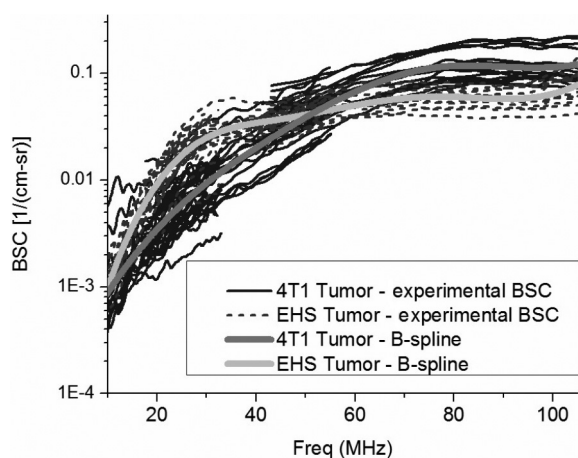


Fig. 7. Experimental BSC versus frequency for 4T1 tumors (thin solid lines) in comparison with EHS tumors (thin dashed lines). Each experimental curve represents the average of 11 image planes from one tumor sample. The two B-spline curves show the trend shapes for the 4T1 (thick dark) and EHS (thick gray), respectively.

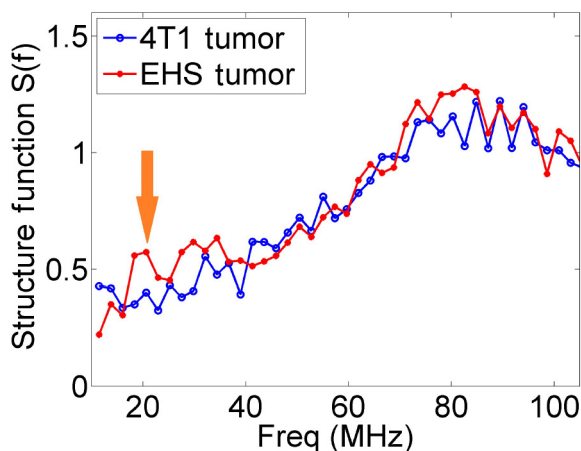


Fig. 8. Structure function estimated from histology for 4T1 tumor and EHS tumor. Each curve is an average of three images.

EHS were significantly different than those of the 4T1 curves (Fig. 7). The increased scattering around 25 MHz for EHS is hypothesized to be caused by the increase in structure function amplitude because of the grouping in the cell distribution. Theoretically, the frequency at which the structure function is increased because of aggregation is related to the size of the aggregate. For the EHS case, the 25-MHz frequency corresponds to a ka value of 2 for a 20- μm radius (aggregate size). To test the above hypothesis, the structure function was estimated from histology for the two tumor types (Fig. 8). The structure function for EHS turns out to be higher than the 4T1 curve in the frequency range of 20–35 MHz (see the arrow in Fig. 8), consistent with the observation in BSC. The BSC behavior observed in Fig. 7 of this paper is consistent with the BSC behaviors presented in the literature. Fig. 1 in [24] represents the computer simulation based on the structure functions for homogeneously distributed red blood cells and aggregated red blood cells. The BSCs from aggregated cells show also an increase in amplitude in the low frequencies.

V. CONCLUSION

The method for estimating the structure function from histology is feasible. Acoustically estimated and histologically estimated structure functions are in reasonable agreement with each other in the shape, suggesting that the acoustically estimated structure function is indeed related to scatterer position distribution. Also, the computer simulations on random distributions of spheres in 3-D suggest that the 2-D structure function could be used to reveal the shape of the 3-D structure function with a good agreement in the frequency position of the structure function peak, but with a bias on the amplitude. Further research is needed for accurately estimating the peak location and magnitude of the 3-D structure function using the 2-D structure function.

ACKNOWLEDGMENT

The authors would like to thank J. R. Kelly, for fabricating the cell pellets, R. J. Miller, DVM, for preparing the tumor samples, S. Sarwate, for tissue and cell morphology discussions, and R. de Monchy and E. Franceschini, for providing the code for simulating 3-D distributions of polydisperse spheres using the Metropolis algorithm.

REFERENCES

- [1] E. J. Feleppa, F. L. Lizzi, D. J. Coleman, and M. M. Yaremko, "Diagnostic spectrum analysis in ophthalmology: A physical perspective," *Ultrasound Med. Biol.*, vol. 12, no. 8, pp. 623–631, 1986.
- [2] D. J. Coleman *et al.*, "Noninvasive in vivo detection of prognostic indicators for high-risk uveal melanoma: Ultrasound parameter imaging," *Ophthalmology*, vol. 111, no. 3, pp. 558–564, 2004.
- [3] E. J. Feleppa *et al.*, "Typing of prostate tissue by ultrasonic spectrum analysis," *IEEE Trans. Ultrason., Ferroelectr., Freq. Control*, vol. 43, no. 4, pp. 609–619, Jul. 1996.
- [4] M. F. Insana, T. J. Hall, J. G. Wood, and Z. Y. Yan, "Renal ultrasound using parametric imaging techniques to detect changes in microstructure and function," *Invest. Radiol.*, vol. 28, no. 8, pp. 720–725, 1993.
- [5] J. G. Miller *et al.*, "Myocardial tissue characterization: An approach based on quantitative backscatter and attenuation," in *Proc. Ultrason. Symp.*, 1983, pp. 782–793.
- [6] P. K. Tamirisa, M. R. Holland, J. G. Miller, and J. E. Perez, "Ultrasonic tissue characterization: Review of an approach to assess hypertrophic myocardium," *Echocardiography*, vol. 18, no. 7, pp. 593–597, 2001.
- [7] L. Y. L. Mo and R. S. C. Cobbold, "Theoretical models of ultrasonic scattering in blood," in *Ultrasonic Scattering in Biological Tissues*, K. K. Shung and G. A. Thieme, Eds. Boca Raton, FL, USA: CRC Press, 1993, ch. 5, pp. 125–170.
- [8] F. T. H. Yu, E. Franceschini, B. Chayer, J. K. Armstrong, H. J. Meiselman, and G. Cloutier, "Ultrasonic parametric imaging of erythrocyte aggregation using the structure factor size estimator," *Biorheology*, vol. 46, no. 4, pp. 343–363, 2009.
- [9] M. L. Oelze, W. D. O'Brien, Jr., J. P. Blue, and J. F. Zachary, "Differentiation and characterization of rat mammary fibroadenomas and 4T1 mouse carcinomas using quantitative ultrasound imaging," *IEEE Trans. Med. Imag.*, vol. 23, no. 6, pp. 764–771, Jun. 2004.
- [10] M. L. Oelze and W. D. O'Brien, Jr., "Application of three scattering models to characterization of solid tumors in mice," *Ultrason. Imag.*, vol. 28, no. 2, pp. 83–96, 2006.
- [11] L. A. Wirtzfeld *et al.*, "Techniques and evaluation from a cross-platform imaging comparison of quantitative ultrasound parameters in an in vivo rodent fibroadenoma model," *IEEE Trans. Ultrason., Ferroelectr., Freq. Control*, vol. 60, no. 7, pp. 1386–1400, Jul. 2013.
- [12] L. A. Wirtzfeld *et al.*, "Quantitative ultrasound comparison of MAT and 4T1 mammary tumors in mice and rats across multiple imaging systems," *J. Ultrasound Med.*, vol. 34, no. 8, pp. 1373–1383, 2015.

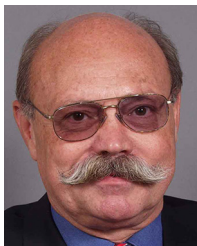
- [13] B. Garra, M. Insana, T. Shawker, R. F. Wagner, M. Bradford, and M. Russell, "Quantitative ultrasonic detection and classification of diffuse liver disease. Comparison with human observer performance," *Invest. Radiol.*, vol. 24, no. 3, pp. 196–203, 1989.
- [14] J. Mamou *et al.*, "Three-dimensional high-frequency backscatter and envelope quantification of cancerous human lymph nodes," *Ultrasound Med. Biol.*, vol. 37, no. 3, pp. 345–357, 2011.
- [15] M. C. Kolios, G. J. Czarnota, M. Lee, J. W. Hunt, and M. D. Sherar, "Ultrasonic spectral parameter characterization of apoptosis," *Ultrasound Med. Biol.*, vol. 28, no. 5, pp. 589–597, 2002.
- [16] B. Banihashemi, R. Vlad, B. Debeljevic, A. Giles, M. C. Kolios, and G. J. Czarnota, "Ultrasound imaging of apoptosis in tumor response: Novel preclinical monitoring of photodynamic therapy effects," *Cancer Res.*, vol. 68, no. 20, pp. 8590–8596, 2008.
- [17] A. Sadeghi-Naini *et al.*, "Quantitative ultrasound evaluation of tumor cell death response in locally advanced breast cancer patients receiving chemotherapy," *Clin. Cancer Res.*, vol. 19, pp. 2163–2174, 2013.
- [18] M. P. Andre *et al.*, "Accurate diagnosis of nonalcoholic fatty liver disease in human participants via quantitative ultrasound," in *Proc. IEEE Int. Ultrason. Symp.*, 2014, pp. 2375–2377.
- [19] S. C. Lin *et al.*, "Noninvasive diagnosis of nonalcoholic fatty liver disease and quantification of liver fat using a new quantitative ultrasound technique," *Clin. Gastroenterol. Hepatol.*, vol. 13, no. 7, pp. 1337–1345, 2015.
- [20] H. Tadayyon, A. Sadeghi-Naini, L. Wirtzfeld, F. C. Wright, and G. Czarnota, "Quantitative ultrasound characterization of locally advanced breast cancer by estimation of its scatterer properties," *Med. Phys.*, vol. 41, no. 1, p. 012903, 2014.
- [21] M. F. Insana, R. F. Wagner, D. G. Brown, and T. J. Hall, "Describing small-scale structure in random media using pulse-echo ultrasound," *J. Acoust. Soc. Amer.*, vol. 87, no. 1, pp. 179–192, 1990.
- [22] V. Twersky, "Low-frequency scattering by correlated distributions of randomly oriented particles," *J. Acoust. Soc. Amer.*, vol. 81, no. 5, pp. 1609–1618, 1987.
- [23] I. Fontaine, M. Bertrand, and G. Cloutier, "A system-based approach to modeling the ultrasound signal backscattered by red blood cells," *Biophys. J.*, vol. 77, no. 5, pp. 2387–2399, 1999.
- [24] E. Franceschini, R. K. Saha, and G. Cloutier, "Comparison of three scattering models for ultrasound blood characterization," *IEEE Trans. Ultrason., Ferroelectr., Freq. Control*, vol. 60, no. 11, pp. 2321–2334, Nov. 2013.
- [25] A. Han and W. D. O'Brien, Jr., "Structure function for high-concentration biophantoms of polydisperse scatterer sizes," *IEEE Trans. Ultrason., Ferroelectr., Freq. Control*, vol. 62, no. 2, pp. 303–318, Feb. 2015.
- [26] L. Y. Mo and R. S. Cobbold, "A stochastic model of the backscattered Doppler ultrasound from blood," *IEEE Trans. Biomed. Eng.*, vol. BME-33, no. 1, pp. 20–27, Jan. 1986.
- [27] L. Y. Mo and R. S. Cobbold, "A unified approach to modeling the backscattered Doppler ultrasound from blood," *IEEE Trans. Biomed. Eng.*, vol. 39, no. 5, pp. 450–461, May 1992.
- [28] J. W. Hunt, A. E. Worthington, A. Xuan, M. C. Kolios, G. J. Czarnota, and M. D. Sherar, "A model based upon pseudo regular spacing of cells combined with the randomisation of the nuclei can explain the significant changes in high-frequency ultrasound signals during apoptosis," *Ultrasound Med. Biol.*, vol. 28, no. 2, pp. 217–226, 2002.
- [29] R. M. Vlad, R. K. Saha, N. M. Alajez, S. Ranieri, G. J. Czarnota, and M. C. Kolios, "An increase in cellular size variance contributes to the increase in ultrasound backscatter during cell death," *Ultrasound Med. Biol.*, vol. 36, no. 9, pp. 1546–1558, 2010.
- [30] M. Teisseire, A. Han, R. Abuhabsah, J. P. Blue, Jr., S. Sarwate, and W. D. O'Brien, Jr., "Ultrasonic backscatter coefficient quantitative estimates from Chinese hamster ovary cell pellet biophantoms," *J. Acoust. Soc. Amer.*, vol. 128, pp. 3175–3180, 2010.
- [31] A. Han, R. Abuhabsah, J. P. Blue, Jr., S. Sarwate, and W. D. O'Brien, Jr., "Ultrasonic backscatter coefficient quantitative estimates from high-concentration Chinese hamster ovary cell pellet biophantoms," *J. Acoust. Soc. Amer.*, vol. 130, pp. 4139–4147, 2011.
- [32] V. Twersky, "Low-frequency scattering by mixtures of correlated non-spherical particles," *J. Acoust. Soc. Amer.*, vol. 84, no. 1, pp. 409–415, 1988.
- [33] D. Savéry and G. Cloutier, "A point process approach to assess the frequency dependence of ultrasound backscattering by aggregating red blood cells," *J. Acoust. Soc. Amer.*, vol. 110, no. 6, pp. 3252–3262, 2001.
- [34] D. Savéry and G. Cloutier, "Effect of red cell clustering and anisotropy on ultrasound blood backscatter: A Monte Carlo study," *IEEE Trans. Ultrason., Ferroelectr., Freq. Control*, vol. 52, no. 1, pp. 94–103, Jan. 2005.
- [35] R. K. Saha and G. Cloutier, "Monte Carlo study on ultrasound backscattering by three-dimensional distributions of red blood cells," *Phys. Rev. E*, vol. 78, p. 061919, 2008.
- [36] R. K. Saha and M. C. Kolios, "Effects of cell spatial organization and size distribution on ultrasound backscattering," *IEEE Trans. Ultrason., Ferroelectr., Freq. Control*, vol. 58, no. 10, pp. 2118–2131, Oct. 2011.
- [37] E. Franceschini and R. Guillermin, "Experimental assessment of four ultrasound scattering models for characterizing concentrated tissue-mimicking phantoms," *J. Acoust. Soc. Amer.*, vol. 132, no. 6, pp. 3735–3747, 2012.
- [38] J. K. Percus and G. J. Yeivick, "Analysis of classical statistical mechanics by means of collective coordinates," *Phys. Rev.*, vol. 110, pp. 1–13, 1958.
- [39] A. Han, R. Abuhabsah, R. J. Miller, S. Sarwate, and W. D. O'Brien, Jr., "The measurement of ultrasound backscattering from cell pellet biophantoms and tumors ex vivo," *J. Acoust. Soc. Amer.*, vol. 134, no. 1, pp. 686–693, 2013.
- [40] J. Mamou, M. L. Oelze, W. D. O'Brien, Jr., and J. F. Zachary, "Identifying ultrasonic scattering sites from three-dimensional impedance maps," *J. Acoust. Soc. Amer.*, vol. 117, pp. 413–423, 2005.
- [41] J. Mamou, M. L. Oelze, W. D. O'Brien, Jr., and J. F. Zachary, "Extended three-dimensional impedance map methods for identifying ultrasonic scattering sites," *J. Acoust. Soc. Amer.*, vol. 123, pp. 1195–1208, 2008.
- [42] N. Xu and E. S. C. Ching, "Effects of particle-size ratio on jamming of binary mixtures at zero temperature," *Soft Matter*, vol. 6, pp. 2944–2948, 2010.
- [43] N. Metropolis, A. W. Rosenbluth, M. N. Rosenbluth, A. H. Teller, and E. Teller, "Equations of state calculations by fast computing machines," *J. Chem. Phys.*, vol. 21, no. 6, pp. 1087–1092, 1953.
- [44] A. Bezrukov, M. Bargiel, and D. Stoyam, "Statistical analysis of simulated random packings of spheres," *Part. Part. Syst. Character.*, vol. 19, no. 2, pp. 111–118, 2002.
- [45] K. F. A. Ross, "Cell shrinkage caused by fixatives and paraffin-wax embedding in ordinary cytological preparations," *J. Microsc. Sci.*, vol. 94, pp. 125–139, 1953.
- [46] T. Tran *et al.*, "Correcting the shrinkage effects of formalin fixation and tissue processing for renal tumors: toward standardization of pathological reporting of tumor size," *J. Cancer*, vol. 6, no. 8, pp. 759–766, 2015.
- [47] M. C. Kolios *et al.*, "An investigation of backscatter power spectra from cells, cell pellets and microspheres," in *Proc. IEEE Int. Ultrason. Symp.*, 2003, pp. 752–757.
- [48] R. E. Baddour, M. D. Sherar, J. W. Hunt, G. J. Czarnota, and M. C. Kolios, "High-frequency ultrasound scattering from microspheres and single cells," *J. Acoust. Soc. Amer.*, vol. 117, no. 2, pp. 934–943, 2005.
- [49] G. J. Czarnota and M. C. Kolios, "Ultrasound detection of cell death," *Imag. Med.*, vol. 2, pp. 17–28, 2010.
- [50] A. D. Pawlicki, A. J. Dapore, S. Sarwate, and W. D. O'Brien, Jr., "Three-dimensional impedance map analysis of rabbit liver," *J. Acoust. Soc. Amer.*, vol. 130, pp. EL334–EL338, 2011.
- [51] M. L. Oelze and J. F. Zachary, "Examination of cancer in mouse models using high-frequency quantitative ultrasound," *Ultrasound Med. Biol.*, vol. 32, pp. 1639–1648, 2006.
- [52] L. R. Taggart, R. E. Baddour, A. Giles, G. J. Czarnota, and M. C. Kolios, "Ultrasonic characterization of whole cells and isolated nuclei," *Ultrasound Med. Biol.*, vol. 22, pp. 389–401, 2007.



Aiguo Han (S'13–M'15) was born in Jiangsu, China, in 1986. He received the B.S. degree in Acoustics from Nanjing University, Nanjing, China, in 2008, and the M.S. and Ph.D. degrees in electrical and computer engineering from the University of Illinois at Urbana-Champaign, Urbana, IL, USA, in 2011 and 2014, respectively.

Since 2015, he has been a Postdoctoral Research Associate with the University of Illinois at Urbana-Champaign. His research interests include ultrasonic wave propagation in heterogeneous media, quantitative ultrasound imaging, signal processing, and computational methods.

Dr. Han is a member of the Acoustical Society of America and a member of the American Institute of Ultrasound in Medicine. He was the recipient of the New Investigator Basic Science Award of the 2016 AIUM Annual Convention.



William D. O'Brien, Jr. (S'64–M'70–SM'79–F'89–LF'08) received the B.S., M.S., and Ph.D. degrees in Electrical Engineering from the University of Illinois at Urbana-Champaign, Urbana, IL, USA.

From 1971 to 1975, he worked with the Bureau of Radiological Health (currently, the Center for Devices and Radiological Health) of the U.S. Food and Drug Administration, Rockvill, MD, USA. In 1975, he joined the faculty at the University of Illinois, where he is currently a Research Professor of Electrical and Computer Engineering and the

Director of the Bioacoustics Research Laboratory, Urbana, IL, USA. He has published more than 393 papers. His research interests include many areas of ultrasound–tissue interaction, including biological effects and quantitative ultrasound imaging.

Dr. O'Brien is a Fellow of the Acoustical Society of America and a Fellow of the American Institute of Ultrasound in Medicine, and is a Founding Fellow of the American Institute of Medical and Biological Engineering. He has served as President (1982–1983) of the IEEE Sonics and Ultrasonics Group (currently the IEEE Ultrasonics, Ferroelectrics, and Frequency Control Society), Editor-in-Chief (1984–2001) of the IEEE TRANSACTIONS ON ULTRASONICS, FERROELECTRICS, AND FREQUENCY CONTROL, and President (1988–1991) of the American Institute of Ultrasound in Medicine. He was the recipient of the IEEE Centennial Medal (1984), the AIUM Presidential Recognition Awards (1985 and 1992), the AIUM/WFUMB Pioneer Award (1988), the IEEE Outstanding Student Branch Counselor Award for Region 4 (1989), the AIUM Joseph H. Holmes Basic Science Pioneer Award (1993), the IEEE Ultrasonics, Ferroelectrics, and Frequency Control Society Distinguished Lecturer Award (1997–1998), the IEEE Ultrasonics, Ferroelectrics, and Frequency Control Society's Achievement Award (1998), the IEEE Millennium Medal (2000), the IEEE Ultrasonics, Ferroelectrics, and Frequency Control Society's Distinguished Service Award (2003), the AIUM William J. Fry Memorial Lecture Award (2007), and the IEEE Ultrasonics, Ferroelectrics, and Frequency Control Society's Rayleigh Award (2008).